Acidic and neutral cesium salts of 12-molybdophosphoric acid supported on SBA-15 mesoporous silica. The influence of Cs concentration and surface coverage on textural and structura…

5 AUTHORS, INCLUDING:

Alexandru Popa
Institute of Chemistry Timisoara, Romania
96 PUBLICATIONS **272** CITATIONS

SEE PROFILE

Viorel Zoltan Sasca
Institute of Chemistry Timisoara-Romanian…
62 PUBLICATIONS **224** CITATIONS

SEE PROFILE

Paul Barvinschi
West University of Timisoara
66 PUBLICATIONS **517** CITATIONS

SEE PROFILE

Ivanka Holclajtner-Antunović
University of Belgrade
99 PUBLICATIONS **428** CITATIONS

SEE PROFILE

Acidic and neutral caesium salts of 12-molybdophosphoric acid supported on SBA-15 mesoporous silica. The influence of Cs concentration and surface coverage on textural and structural properties

Alexandru Popa [a,*], Viorel Sasca [a], Orsina Verdes [a], Paul Barvinschi [b], Ivanka Holclajtner-Antunović [c]

[a] Institute of Chemistry Timişoara, Bl. Mihai Viteazul 24, 300223 Timisoara, Romania
[b] Faculty of Physics, West University of Timisoara, B-dul V. Parvan, Nr. 4, 300223 Timisoara, Romania
[c] Faculty of Physical Chemistry, University of Belgrade, P.O. Box 47, 11158 Belgrade, Serbia

ABSTRACT

The Cs salts of molybdophosphoric acid $Cs_1H_2PMo_{12}O_{40}$ (Cs_1PM) and $Cs_3PMo_{12}O_{40}$ (Cs_3PM), were supported on SBA-15 in the concentration of 20, 30 and 40 wt.% loadings. Because Cs salts are insoluble, the SBA-15 supported Cs-acid salts were prepared by two-step sequential impregnation and in situ reaction on the support. The structure and texture of these CsPM/SBA-15 composites were studied by XRD, SEM-EDS, FT-IR and micro-Raman spectroscopy, UV–vis-DRS and N_2 adsorption. Thermal stability was investigated by thermo gravimetric analysis (TGA), differential thermal analysis (DTA) and differential scanning calorimetry (DSC). The acidity of composites was studied by the adsorption of ammonia and its temperature programmed desorption – TPD using thermogravimetry. The evolved gases during the adsorption–desorption of ammonia on CsPM/SBA-15 composites were identified by online mass spectrometry coupled with thermal gravimetry technique. FT-IR and Raman studies demonstrated that CsPM maintained its Keggin structure after deposition on mesoporous SBA-15, regardless of the active phase concentration. For both $Cs_1H_2PMo_{12}O_{40}$ and $Cs_3PMo_{12}O_{40}$-SBA-15 composites could be observed an important increase of band gap energy in comparison with pure salts. The values of specific surface area of pure CsPM were increased by deposition on mesoporous silica support. The immobilization of CsPM on mesoporous SBA-15 obviously increases the thermal stability and the total acidity of the strong acidic sites of the Keggin structures in comparison with their parent bulk Cs salts.

1. Introduction

Among the variety of catalytic systems, heteropolyacids (HPAs) with Keggin structure unsupported and supported on different materials have received much interest in the area of acid and oxidation catalysis due to their acidic and redox properties, which can be controlled at molecular level [1–5].

HPAs and particularly heteropolymolybdates are used as oxidation catalysts due to the relatively high oxidation ability of molybdenum ions. However, these HPAs are also associated with some limitations such as low surface area, relatively low thermal stability and high solubility in water and polar solvents. In order to

enhance these properties HPAs are usually impregnated on different porous materials with high surface area (hexagonal mesoporous silica, titania, carbon, zirconia, polymers, molecular sieves) [6–10].

During the last decades HPAs supported on mesoporous siliceous materials MCM-41 and SBA-15 have attracted much attention due to their very high surface area coupled with regular hexagonal array of uniform pore sizes within the mesoporous region. SBA-15 is a suitable support for acid catalysts as compared with MCM-41 possesses thicker pore walls, larger pore sizes and higher thermal and hydrothermal stability.

It is known that HPAs are strong and useful solid acids, but the amount of acidic sites on their surface is small because of their low surface area. Therefore, increasing the amount of surface acidic sites is an important task for the development of useful solid acids applied in different catalyzed reactions. Different attempts have

been made to improve the efficiency of the HPAs by their supporting on various high surface area matrices and by replacement of protons with alkali metals [11–18].

Very few references have been reported concerning $H_3[PMo_{12}O_{40}]$ and $H_4[PMo_{11}VO_{40}]$ supported on mesoporous materials, majority of the studies have been focused on investigation of the most acidic HPA in the series, namely $H_3PW_{12}O_{40}$ (HPW) [19–26].

Yang et al. [22] have studied HPW immobilized into SBA-15 by sol–gel technique. The hydrothermal stability of composites which was studied by washing the samples with an $EtOH/H_2O$ mixture increased in comparison with parent HPW. The sol–gel derived composite is more stable in the acidic property and the structural regularity of the mesoporous material than the impregnated sample. Palcheva et al. [6] have studied the effect of nickel salt of 12-tungstophosphoric acid, $Ni_{3/2}PW_{12}O_{40}$, as oxide precursors and of hetero-atoms modifying SBA-15 on the activity of NiW/(Al-, Ti-, W-) SBA-15 catalysts in thiophene hydrodesulphurization reaction. The NiW catalyst supported on W-containing SBA-15 showed higher performance in the HDS of thiophene as compared to the SBA-15 modified with Al and Ti. A series of Mo (W) catalysts promoted by Ni and supported on SBA-15 were prepared using Keggin-type heteropolyacids as active phase precursors. It was found that both Mo and W catalysts prepared from heteropolyacids showed better performance in hydrodesulphurization of 4,6-dimethyldibenzothiophene than the counterparts prepared from traditionally used Mo (W) ammonium salts [24]. HPM was successfully encapsulated into the super cage of Y zeolite promoted by Cs counter cation in zeolite matrix, using 2.5% aqueous solution of Cs_2CO_3. The 30% HPM-CsY catalyst exhibits considerable catalytic activity in liquid phase esterification of acetic acid with n-butanol under the optimal reaction conditions [26].

By substitution of H^+ protons with alkali cations, important modifications take place on the surface area, pore structure, solubility and hydrophobicity, in comparison to the parent HPA. HPAs salts with large monovalent ions, such as NH_4^+, K^+, Rb^+, Cs^+, Ag^+ and Tl^+, are practically insoluble in water or other polar solvents and possess high surface areas [27]. The higher surface area, mainly arising from microporosity observed for caesium salts with Cs/W ratio of >2 compensates the loss of acidic protons. It is supposed that in salts with number of counter ions (which replaces hydrogen ions) $x < 2$, acidic salt is a heterogeneous mixture of microporous neutral salt and unreacted acid; in salts with $x > 2$ the salts are composed of grains with crystalline core of neutral salt covered by surface layer of unreacted acid [28–31].

Partial substitution of protons by these cations may result in changes of the number of available surface acidic sites. For example, the salt $Cs_{2.5}H_{0.5}PW_{12}O_{40}$ was reported as superior catalyst which exhibit significantly higher activity than the parent acid in gas phase acid-catalyzed reactions [32]. However, the caesium salt of HPA forms colloidal suspension in polar media causing filtration problems. This drawback could be overcome by stabilizing Cs salt of HPA in a porous support.

A major disadvantage of HPAs salts with big cations consists in their insolubility which makes impossible the conventional aqueous impregnation on different supports. In order to overcome this disadvantage, a sequential impregnation was used and in situ reaction on two types of supports: silica and γ-Al_2O_3 [11]. $Cs_{2.5}H_{0.5}PW_{12}O_{40}$ heteropolyacid salt prepared by the same technique by deposition of the parent salt on SBA-15 support was studied by Rao et al. As Cs acid salts are insoluble, the SBA-15 supported Cs-acid salt was prepared by two-step sequential impregnation and in situ reaction on the support [16]. Silica supported ammonium salt of 12-molybdophosphoric acid catalysts has been investigated by Gong et al. on liquid nitration of

benzene with 65% nitric acid as nitrating agent [33]. These catalysts with different loadings were prepared by sol–gel method and supported catalysts had high nitration reaction catalytic activity and selectivity over nitrobenzene.

In the past decades different HPAs salts (especially of HPW acid) based on only one type of cation or mixed salts have been extensively reported, but the influence of cation concentration and of the surface coverage of Cs salts of 12-molybdophosphoric supported on SBA-15 in reference to the bulk solid HPM have not been significantly studied in the literature.

In this study was carried out the preparation of the Cs salts of molybdophosphoric acid $Cs_1H_2PMo_{12}O_{40}$ (Cs$_1$PM), and $Cs_3PMo_{12}O_{40}$ (Cs$_3$PM), by supporting on SBA-15 molecular sieve, in the concentration of 20, 30 and 40 wt.% loading. The goal of this work was to characterize the texture, structure and the influence of Cs concentration and surface coverage of these heteropolyacids salts in reference to the bulk solid heteropolyacids. The amount and strength of the acidic sites were calculated by desorption of ammonia, measured by thermal analysis. For the clarity of discussion, some data obtained for $Cs_{2.5}H_{0.5}PMo_{12}O_{40}$ samples presented in our previous paper [34] are also given.

2. Experimental

2.1. Samples preparation

The bulk CsPM with Cs/Keggin unit (KU) ratio of 1 and 3 were prepared by adding slowly drop wise the required amount of aqueous caesium nitrate $CsNO_3$ to aqueous $H_3PMo_{12}O_{40}$ with vigorous stirring at room temperature. The precipitates obtained were aged in parent solution for 24 h at room temperature, followed by evaporation in vacuum at 50 °C, and finally calcination at 300 °C for 4 h.

The CsPM/SBA-15 composites were synthesized as follows: first caesium nitrate was impregnated by aqueous incipient wetness onto SBA-15 molecular sieve, dried and calcined at 300 °C and finally 12-molybdophosphoric acid was impregnated by a similar aqueous impregnation route. The detailed preparation procedure was given in our previous paper [34].

Two types of Cs salts of molybdophosphoric acid ($Cs_1H_2PMo_{12}O_{40}$ (Cs$_1$PM), and $Cs_3PMo_{12}O_{40}$ (Cs$_3$PM)), were deposited in the concentration of 20, 30 and 40 wt.% concentration loadings.

Mesoporous silica SBA-15 was synthesized according to the procedure developed by Zhao et al. by the hydrolysis of tetraethyl orthosilicate (TEOS) using a P123 block copolymer as surfactant [35,36].

The structure and texture of CsPM supported on SBA-15 were studied by XRD, FT-IR and micro-Raman spectroscopy, SEM-EDX and low temperature nitrogen adsorption technique. Thermal stability was studied by TG–DTA and DSC methods.

2.2. Measurements of textural properties

Textural characteristics of the outgassed samples were obtained from nitrogen physisorption using a Quantachrome instrument, Nova 2000 series. The specific surface area S_{BET}, average cylindrical pore diameters d_p and adsorption pore volume V_{pN2} were determined. Prior to the measurements the samples were degassed to 10^{-5} Pa at 250 °C. The BET specific surface area was calculated by using the standard Brunauer, Emmett and Teller method on the basis of the adsorption data. The pore size distributions were calculated applying the Barrett–Joyner–Halenda (BJH) method to the desorption branches of the isotherms. The IUPAC classification of pores and isotherms were used in this study.

2.3. XRD analysis

Powder X-ray diffraction patterns were obtained with a Bruker D8 Advance diffractometer using the Cu Kα radiation (Ni filter on the diffracted beam, 40 kV and 40 mA) in a Bragg–Brentano geometry, with Soller and fixed slits and a NaI (Tl) scintillation detector, at small angles (2θ = 0.5–5°) and wide angles (2θ = 5–60°) respectively.

2.4. Surface characterization by Fourier transform infrared (FT-IR) spectroscopy and micro-Raman spectroscopy

The FT-IR absorption spectra were recorded with a Jasco 430 spectrometer (spectral range 4000–400 cm^{-1} range, 256 scans, and resolution 2 cm^{-1}) using KBr pellets.

The micro-Raman spectra of polycrystalline samples were recorded on a Thermo DXR Raman microscope, using the 532 nm excitation line from a diode pumped, solid state laser, with a constant power of 0.7 mW and spot size of 0.7 μm on the sample. Due to the thermal sensitivity of molybdophosphates it is very important to record spectra applying low laser power to avoid sample destruction. The spectra were recorded using 25 μm pinhole confocal aperture, with 10 s exposure and 10 repetitions. The spectral resolution of all the measured spectra was 2 cm^{-1}. The data were collected at room temperature.

2.5. UV–vis diffuse reflectance spectra

The UV–vis diffuse reflection spectra of heteropoly compound samples were measured on a Lambda 950 Perkin-Elmer spectrometer with integrating sphere. Approximately 100 mg wafers were placed in a chamber operating under atmospheric pressure. The diffuse reflectance data were evaluated using the Kubelka–Munk equation.

2.6. Thermal analysis

Thermal analysis was carried out using a TGA/SDTA 851-LF 1100 Mettler apparatus. The samples with mass of about 20 mg were placed in alumina crucible of 150 μl. The measurements were performed in dynamic air atmosphere with the flow rate of 50 ml min^{-1}, in the temperature range of 25–650 °C with a heating rate of 10 °C min^{-1} and isothermal heating at 350 °C for 60 min.

DSC analysis was carried out with a Mettler Star system DSC 823 apparatus. The samples with mass of 20–40 mg were placed in Pt crucible of 150 μl. The measurements were performed in dynamic air atmosphere with the flow rate of 50 ml min^{-1}, in the temperature range of 30–700 °C with a heating rate of 10 °C min^{-1}.

2.7. Temperature programmed desorption

Temperature programmed desorption (TPD) of ammonia was carried out with a Mettler TGA/SDTA 851/LF/1100 thermo analyser adapted for simultaneous TG/DTG–DTA analysis. The thermal analysis system was coupled with a Pfeiffer-Vacuum-Thermo Star mass spectrometer by silica capillary at temperature of 200 °C. About 20 mg samples were used for measurements using the alumina crucibles of 150 μl volume.

Prior to TPD studies at 100 °C, the catalyst sample was treated at 300 °C for 1 h by passing pure air and than cooling from 300 to 100 °C, under nitrogen flow. After pretreatment, the sample was saturated with ammonia (10% NH$_3$–90% N$_2$ mixture gas) at 100 °C at a flow rate of 50 ml min^{-1} for 2 h and was subsequently flushed with N$_2$ at the same temperature to remove physisorbed ammonia. The desorption of ammonia is followed by non-isothermal heating from 100 to 600 °C, with 10 °C min^{-1}, under nitrogen flow of 50 ml min^{-1}. Finally, an isothermal heating at 600 °C, under 50 ml min^{-1} of air flow is used, in order to check up the formation of organic deposits on heteropoly compounds.

TPD of ammonia was employed to measure the amount and strength of the acidic sites of the catalysts. The amount of NH$_3$ evolved was calculated from the mass loss of the samples observed on TG–DTG curves.

2.8. Scanning electronic microscopy (SEM) and EDX analysis

Microstructure characterization of the catalyst particles was carried out with a JEOL JSM-6610LV scanning electron microscope (SEM) connected with an INCA energy-dispersion X-ray analysis (EDX) unit with resolution of 0.126 keV. An acceleration voltage of 20 kV was used for the images. Powder materials were deposited on adhesive tape fixed to specimen tabs and then ion sputter coated with gold.

3. Results and discussion

3.1. Porosity and surface area

The nitrogen adsorption–desorption isotherms of Cs$_1$PM/SBA-15 and Cs$_3$PM/SBA-15 composites at different wt.% loadings and the parent mesoporous silica SBA-15 are displayed in Figs. 1 and 2. All these isotherms exhibit a typical adsorption curve of type IV according to IUPAC classification. These isotherms exhibit hysteresis loops of H1 type at a relative pressure of p/p_0 = 0.4–0.9. Hysteresis appearing in the multilayer range of physisorption isotherms is usually associated with capillary condensation in mesopore structures. The shapes of hysteresis loops have often been related to specific pore structures. In our case the hysteresis type H1 is associated with porous materials known to consist of agglomerates or compacts of approximately uniform spheres in fairly regular array, and hence to have a narrow distribution of pore size [37].

The results of textural characteristics analysis (BET surface area, BJH pore diameter and average pore volume) for different composites are given in Table 1. For parent Cs$_1$PM, and Cs$_3$PM a narrow hysteresis loop is observed (not shown). The bulk CsPM salts displayed surface area varying from 6.1 m^2/g (Cs$_1$H$_2$PMo$_{12}$O$_{40}$) to 138 m^2/g (Cs$_3$PMo$_{12}$O$_{40}$) and a pore volume below 0.1 cm^3/g for both unsupported CsPM salts.

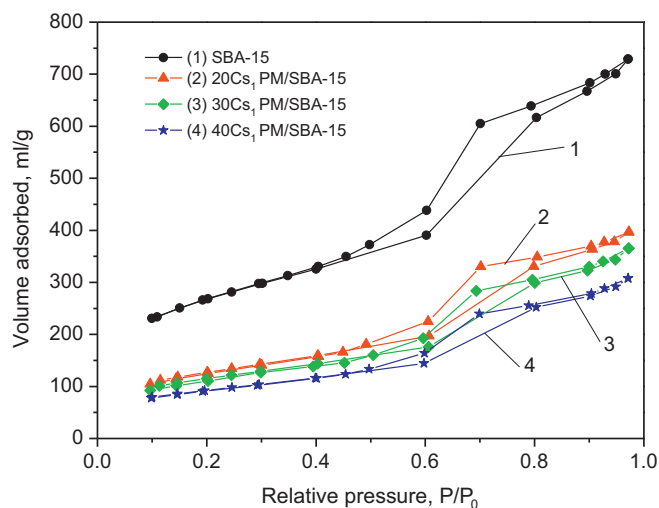**Fig. 1.** Nitrogen adsorption–desorption isotherms of Cs$_1$H$_2$PMo$_{12}$O$_{40}$ supported on SBA-15 at different wt.% loading.
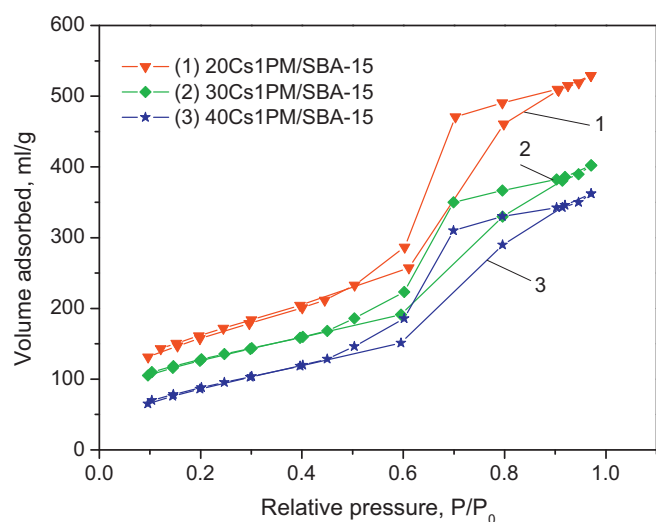
Fig. 2. Nitrogen adsorption–desorption isotherms of $Cs_3PMo_{12}O_{40}$ supported on SBA-15 at different wt.% loading.

Fig. 3. (a) X-ray diffraction pattern of $Cs_1PM/SBA-15$ composites and (b) X-ray diffraction pattern of $Cs_3PM/SBA-15$ composites.

By supporting the CsPM salts on SBA-15, the resulting composites have shown both increased surface areas and pore volume. The surface areas of the supported composites were relatively high and ranged from 320 to 570 m^2/g.

The pore size distribution curves of parent mesoporous silica SBA-15 have narrow pore size distribution within mesopore range with a maximum at 6.2 nm (not shown). The pore size distribution curves of CsPM/SBA-15 composites have one maximum within mesopore range between 6.04 nm for $40Cs_3PM/SBA-15$ and 6.20 nm in the case of both 20 $Cs_1PM/SBA-15$ and $20Cs_3PM/SBA-15$.

Generally, after HPAs incorporation in different mesoporous silicas, the surface area, pore volume and pore diameter of initial silica support decreased with increased concentration of active phase loading. Our results show that by impregnation of Cs salts onto SBA-15, the surface area of active CsPM phase is enhanced substantially, but the surface area of obtained composites decrease with increasing CsPM loadings. However, the high surface area above 550 m^2/g could be retained for $20Cs_3PM/SBA-15$. The surface area, pore volume and pore diameter of CsPM/SBA-15 composites decreases with CsPM loading due to the partial blockage of the mesopores of the support by CsPM particles.

3.2. X-ray diffraction

The XRD patterns at small angles for the initial mesoporous silica SBA-15 show three Bragg peaks below 2.0° (2θ) (Fig. 3a and b) indicating its well-ordered two-dimensional mesostructure [35]. These three strong peaks at 0.96°, 1.62° and 1.83° with d-spacings of 92.5, 54.7 and 48.4 Å respectively, were indexed as the 1 0 0,
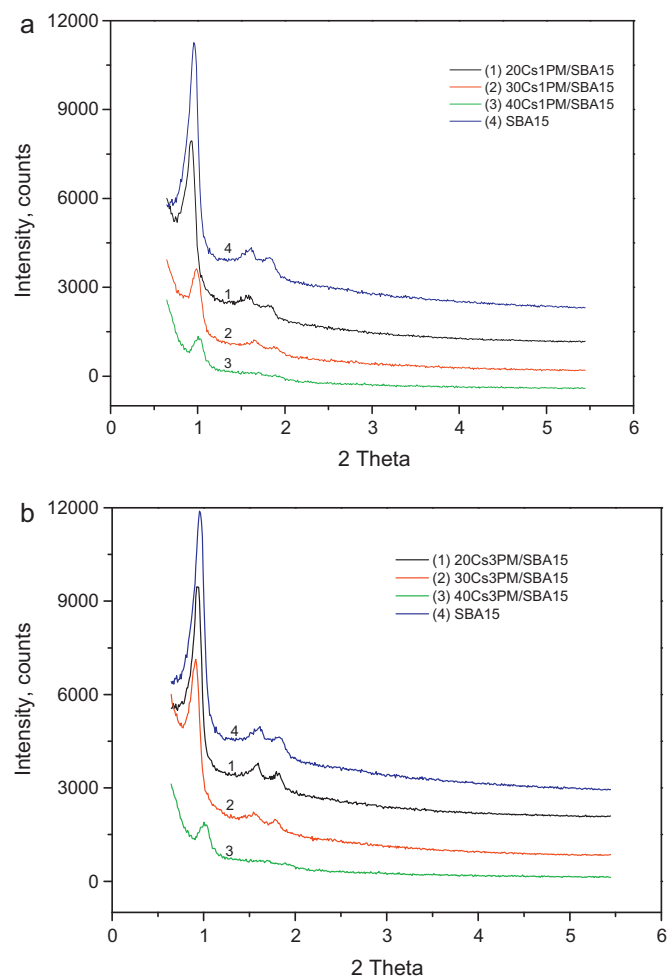
1 1 0 and 2 0 0 reflections associated with the hexagonal structure. Fig. 3a and b shows that the peaks at small angles assigned to SBA-15 appear also for CsPM/SBA-15 composites with different Cs concentration and CsPM loadings, indicating that they preserve the mesopore structure well, with well dispersed CsPM on the surface of the pore walls for SBA-15.

As in the case of $Cs_{2.5}PM/SBA-15$ [34], for both Cs_1PM and $Cs_3PM/SBA-15$ composites the Bragg peaks at small angles are present, but with lower intensity, and slightly shifted to higher angle values. Because the intensity of Bragg peaks diminishes with the increase in loading of active phase, it can be supposed that the decrease in intensity may be related to the presence of interfering scattering due to the presence of the Cs salt active phase or to the partial blocking of the pores by the CsPM salts. Also, it can be

Table 1
Textural properties of $Cs_{3-x}H_xPMo_{12}O_{40}/SBA-15$ composites ($x = 0$; 2).

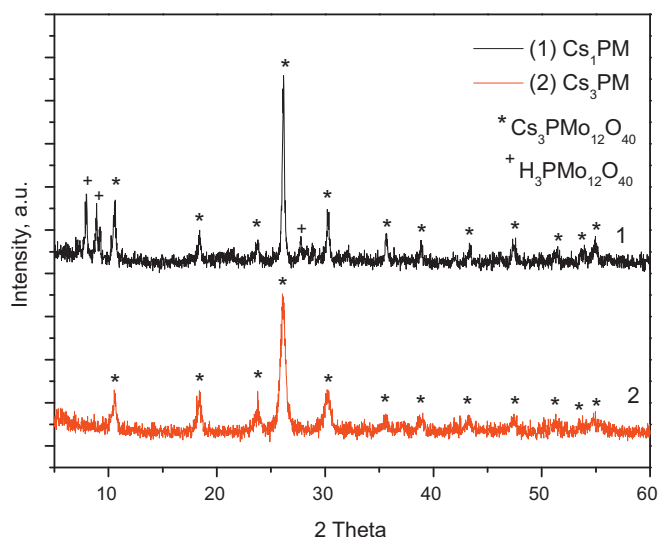| Sample	Specific surface area (m^2/g)	Pore volume BJH_{Des} (ml/g)	Average pore diameter BJH_{Des} (nm)
Mesoporous silica SBA-15	725.0	1.1	6.2
Cs_1PM	6.1	0.01	3.8
20 $Cs_1PM/SBA-15$	440.2	0.6	6.2
30 $Cs_1PM/SBA-15$	396.9	0.6	6.2
40 $Cs_1PM/SBA-15$	321.2	0.5	6.1
Cs_3PM	138.0	0.1	2.9
20 $Cs_3PM/SBA-15$	568.1	0.8	6.2
30 $Cs_3PM/SBA-15$	442.8	0.6	6.2
$40Cs_3PM/SBA-15$	391.9	0.5	6.0

Fig. 4. Wide angles X-ray diffraction patterns for pure Cs_1PM and Cs_3PM.

asserted that the long-range order of mesoporous silica is decreased more evidently for a higher loading of 40 wt.% CsPM/SBA-15 composites. The decrease of long-range order of mesoporous silica especially for higher loadings is due to the active phases that did not disperse uniformly on SBA-15 surface, and which probably block partially the pores, leading to the decrease in SBA-15 porosity and as a consequence the mesostructure ordering decrease. The decreasing porosity of CsPM–SBA-15 composites in comparison with parent support is evidenced from the N_2 adsorption/desorption measurements.

The wide angles ($2\theta = 5$–$60°$) patterns for pure Cs_1PM and Cs_3PM are shown in Fig. 4. The XRD pattern of the $Cs_3PMo_{12}O_{40}$ (reference code: 046-0481) was well matched with the pattern assigned by the JCPDS cards. The patterns of crystalline phases of both Cs_3PM and parent HPM could be found in the XRD of pure Cs_1PM. This is in agreement with the microstructure model which supposes that acidic salts of HPAs containing molybdenum or tungsten are a mixture of neutral salt and parent heteropolyacid. For instance acidic salt $Cs_xH_{3-x}PW_{12}O_{40}$ ($Cs_xH_{3-x}PW$) aggregates have a core of Cs_3PW embedded by H_3PW layers [38,39]. No peak of Cs_3PM crystalline phase was found in the wide angles patterns of both $20Cs_1PM$ and $20Cs_3PM$/SBA-15 composites, which indicated that for low loadings the Cs_3PM clusters were highly dispersed in the mesoporous SBA-15 framework (not shown). By increasing the Cs_1PM and Cs_3PM content, the peaks of the crystalline phase of Cs_3PM became noticeable.

3.3. FTIR and Raman spectrometry

The influence of Cs concentration and surface loadings of CsPM species on SBA-15 matrix was studied by FT-IR and Raman spectrometry (Figs. 5a, b and 6a, b).

In order to confirm the presence of the Keggin anion on CsPM/SBA-15 composites, the samples were analyzed by FT-IR and Raman spectroscopy. The $PMo_{12}O_{40}^{3-}$ Keggin ion structure consists of a PO_4 tetrahedron surround by four Mo_3O_{13} units formed by edge-sharing octahedra. These groups are connected each other by corner-sharing oxygen. This structure give rise to four types of oxygen, being responsible for the fingerprints bands of Keggin ion between 1200 and 700 cm^{-1} [40].

The parent Cs salts, Cs_1PM and Cs_3PM show an IR spectrum containing the main vibrations at 1064–1066 cm^{-1}, 967–970 cm^{-1}, 867–868 cm^{-1}, 791–798 cm^{-1} assigned to the stretching vibrations ν_{as} P–O_a, ν_{as} Mo=O_d, ν_{as} Mo–O_b–Mo and ν_{as} Mo–O_c–
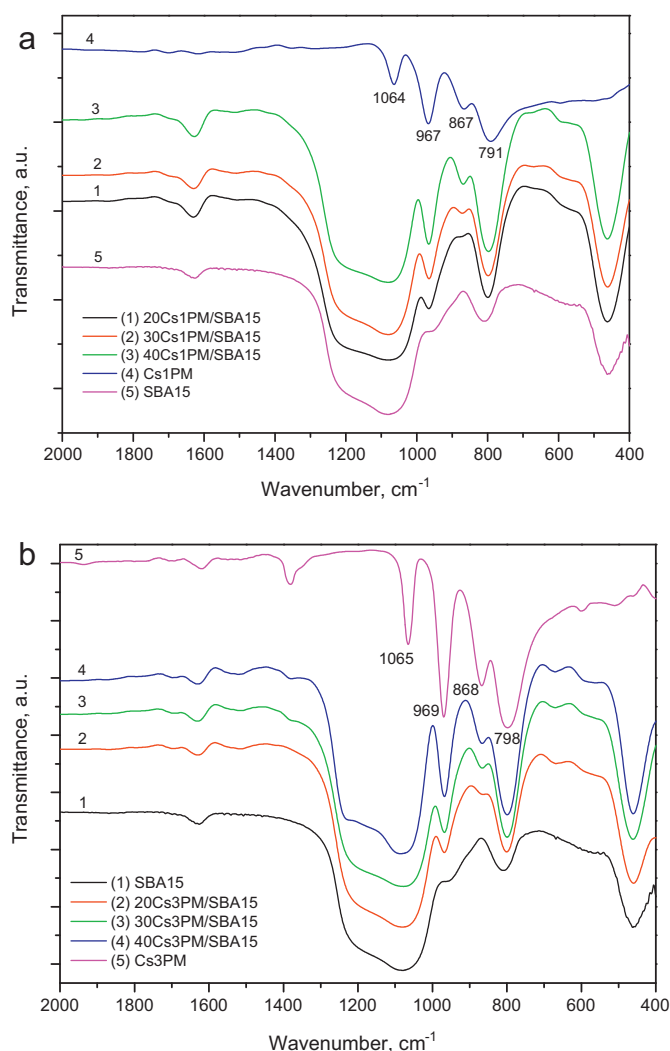

Fig. 5. (a) FTIR spectra of Cs_1PM/SBA-15 composites and (b) FTIR spectra of Cs_3PM/SBA-15 composites.

Mo corresponding to the Keggin structure [41,42]. Some of these bands are preserved in the supported samples, but they are broadened and partially overlapped because of the strong absorption bands of silica from SBA-15 (1090, 800 and 465 cm^{-1}) (Fig. 5a and b).

By introduction of Cs salts of HPM heteropolyacid into the SBA-15 matrix it could be observed an important influence on the structure of resulted composites. Thus the bands of CsPM supported on SBA-15 in the 1300–400 cm^{-1} region are partially or completely overlapped by the bands of the silica matrix. The band assigned to the P–O asymmetric stretching vibration at 1064–1066 cm^{-1} is completely overlapped for both CsPM salts by the strong band at 1090 cm^{-1} of the silica. Three main bands of Cs_1PM and Cs_3PM are distinguishable between 700 and 1000 cm^{-1} on CsPM/SBA-15 composites but they are slightly shifted to higher wavenumbers. One strong band appeared in the spectra of CsPM/SBA-15 composites at 967–970 cm^{-1} which correspond to ν_{as} Mo=O_d vibration band of pure HPM. A band with moderate intensity was observed at 867–868 cm^{-1} especially for Cs_3PM/SBA-15 composites and as a shoulder for Cs_1PM/SBA-15 composites which corresponds to the ν_{as} Mo–O_c–Mo vibration of the HPM. The band corresponding to ν_{as} Mo–O_b–Mo vibration band at 791–798 cm^{-1} is overlapped by strong absorption band of silica from 800 cm^{-1}.
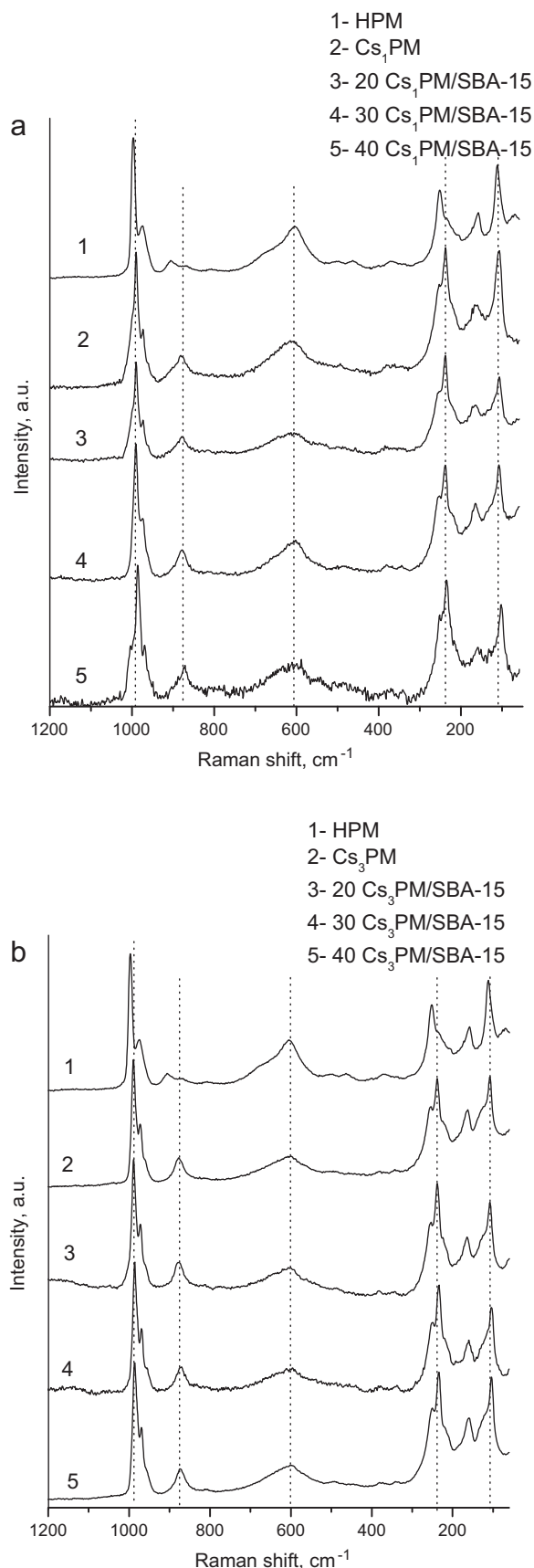
Fig. 6. (a) Raman spectra of Cs$_1$PM/SBA-15 composites and (b) Raman spectra of Cs$_3$PM/SBA-15 composites.

It can be observed that for higher loadings of active phase (30 and 40%), the composites samples exhibit sharper IR bands, while for both 20Cs$_1$PM/SBA-15 and 20Cs$_3$PM/SBA-15 samples exhibit smaller IR bands even a shoulder in the case of ν_{as} Mo–O$_c$–Mo vibration. So, for low loadings of active phase it could be supposed that active phase was more homogeniously dispersed inside the composite pores than for higher loadings of active phase.

Taking into account previously reported FT-IR spectra for Cs$_{2.5}$HPM samples [34], it can be stressed that in all studied composites of Cs salts, the Keggin structure is preserved independently of Cs concentration and surface loadings.

Raman spectra of Cs$_1$PM/SBA-15 and Cs$_3$PM/SBA-15 composites are shown in Fig. 6a and b. The spectra of HPM and unsupported salts Cs$_1$PM and Cs$_3$PM are given for comparison. The Raman spectrum of HPM is in accordance with the previously published results [34,43]. When protons are replaced by large cations, such as Cs, changes in the structure are evidenced by the changes in Raman spectrum. There is a slight shift of the main bands towards lower frequencies in the case of both acid and neutral CsPM salts related to the parent acid. The main characteristic features of the Cs$_1$PM structure are observed at 992 cm^{-1} (ν_s Mo–O$_d$), 973 cm^{-1} (ν_{as} Mo–O$_d$), 878 cm^{-1} (ν_{as} Mo–O$_b$–Mo), 606 cm^{-1} (ν_s Mo–O$_c$–Mo), 241 cm^{-1} (ν_s Mo–O$_a$ with an important bridge stretching character according Ref. [42]), 163 cm^{-1} and 111 cm^{-1}. It is shown in literature [42] that anion–anion interactions of electrostatic type correlated with the cation size are responsible for these changes. It is obvious that the replacement of proton in HPM with big counterion, Cs, causes the decrease in M–O$_d$ stretching frequencies (Fig. 5a and b). The band at about 240 cm^{-1}, assigned roughly to ν_s Mo–O$_a$, undergoes as well a decrease, which can be also related to a decrease of anion–anion interaction. The frequency of other vibrations depends on counterion size as well but in less extent.

In Raman spectra, SBA-15 presents no bands hindering characterization of CsPM. At all applied loadings of CsPM, the Raman spectra are almost identical to that of CsPM, as seen in Fig. 5a and b. There is a slight frequency decrease with respect to unsupported CsPM due to the lower anion–anion interactions in the supported samples.

In Raman spectra of all supported samples there is the broad band about 1600 cm^{-1} which originates from water adsorbed in mesopore structure of molecular sieve. After thermal treatment at 250 °C, the Raman spectrum of SBA-15 loaded with Cs salts shows only slight modifications; the Raman signals are slightly sharper which can be a consequence of higher crystallinity of the composites, while band about 1600 cm^{-1} completely disappears after calcination (not shown).

From these results it is obvious that the Keggin unit is unambiguously preserved for all applied coverage. The slight decrease in Raman frequency ν_s Mo–O$_b$ (from 989 to 986 cm^{-1}) in supported Cs$_3$PM/SBA-15 samples indicates interaction of Keggin unit with the support.

3.4. UV–vis-DRS measurements

The UV–vis diffuse reflectance spectra were transformed in the Kubelka–Munk function vs. wavelength for pure Cs salts and all CsPM/SBA-15 composites as can be seen in Fig. 7a and b.

In the diffuse reflectance spectra of pure heteropoly acids the main absorption band in the UV–vis range is due to the ligand-metal charge transfer (LMCT): O^{2-} → Mo^{6+}. This type of band is usually observed between 200 and 400 nm [44].

For parent H$_3$PMo$_{12}$O$_{40}$, this band is broadened and it has splitted in two bands with maxima at 302 nm and 392 nm (not shown). Both Cs$_1$PM and Cs$_3$PM present the LMCT band with the maximum within range of 305–312 nm but the second maximum of LMCT band has disappeared for Cs$_3$PM, while for acidic salt
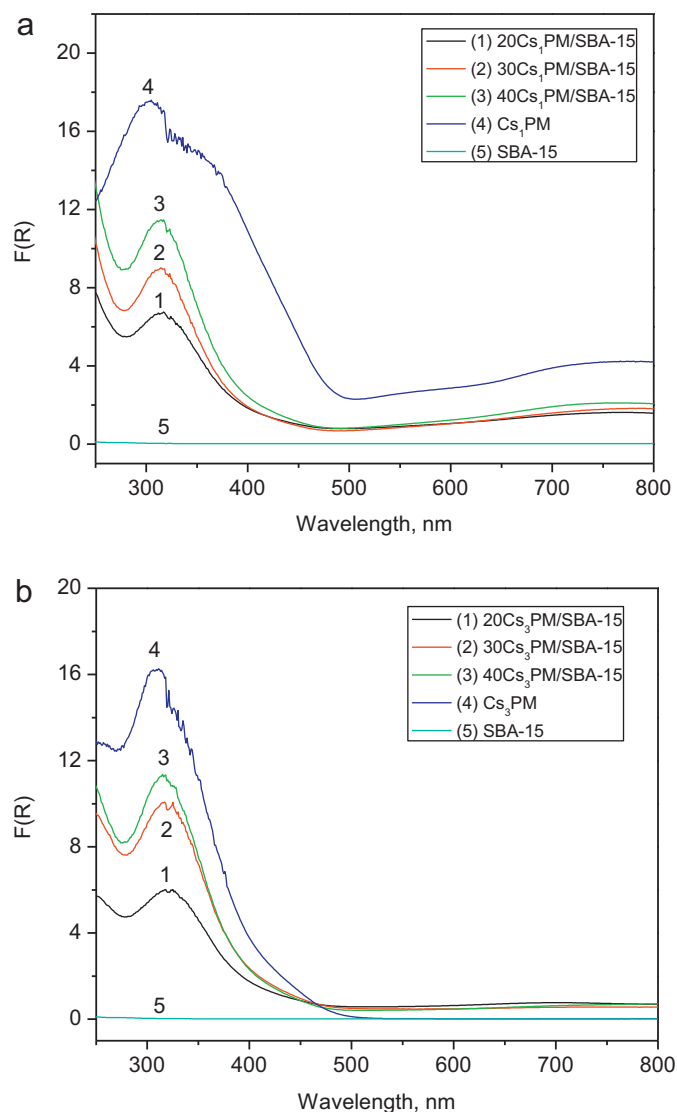
Fig. 7. (a) Kubelka–Munk function vs. wavelength of Cs_1PM/SBA-15 composites and (b) Kubelka–Munk function vs. wavelength of Cs_3PM/SBA-15 composites.

Cs_1PM it appeared like a shoulder (Fig. 7a and b). According to Fournier et al. [44] these results are in accordance with the statement that the LMCT band shifts towards higher wavelength and it broadens when the size of the counter-ion decreases (H^+), i.e. when their polarization power increases and the relative distance between heteropolyanions decreases (this is the case for parent $H_3PMo_{12}O_{40}$ – when the band is broadened and it has splitted in two bands). Unlike in the HPA salts containing bigger counter-ion (Cs^+), the polarization action is lower and as a consequence, the heteropoly anions are isolated one from another in function of the counter-ion size (is the case for Cs salts when only one band is observed).

The profile of Kubelka–Munk function vs. wavelength curves for SBA-15 supported Cs salts is different in comparison with pure salts, as in the low-frequency region of visible spectrum the absorption band becomes narrower being developed between 290 and 350 nm (Fig. 7a and b). The profile of absorption band of SBA-15 supported Cs salts is very similar with the absorption band observed on UV–vis spectra of ammonia salts of HPAs [44].

The LMCT band between 290 and 350 nm of Cs salts supported on SBA-15 is narrower than in the case of pure Cs salts owing to the effect of the support which spreads the KU even at high loadings

and thus decreases the interactions between KUs. This assumption is sustained by Fournier et al. [44,45] for silica supported $H_4SiMo_{12}O_{40}$ which showed that polyanion structure is maintained on the support. On the other hand, Brückman et al. [46] claimed that at low coverage (10–20 wt.% HPA), the system HPA-silica may be considered as composed of KU partially 'immersed' in the hydration layer at the silica surface. It could be supposed that by opening of the Keggin anion structure and formation of a flat structure, the KU protons will have a lower polarizing effect as a result of its interaction with SiO_2.

In order to find out the band gap energy (E_g) value, the position of the adsorption edges was determined by finding the energy intercept of a straight line fitted through the low energy rise in the graphs of $[F(R) \cdot E]^2$ vs. E type (where $F(R)$ is the Kubelka–Munk function and E is the energy of the incident photon) (Fig. 8) [47]. So, the energy values for points of intersection between fitted line and the horizontal axis are the band gap energies – E_g shown in Table 2.

For both Cs_1PM and Cs_3PM/SBA-15 composites one could be observed an important increase of band gap energy in comparison with pure salts, which could be attributed according to the literature, to a structural distortion of the HPAs network due to support interaction or/and due to lower polarizing effect of the KU protons (only for Cs_1PM/SBA-15 composites) as they are partially 'immersed' in the hydration layer at the silica surface [45,46].

Thermal treatment leads to a decrease of E_g values for both supported and unsupported CsPM. Thus, in the temperature range 30–250 °C decreasing of E_g for 20 Cs_1PM/SBA-15 is 0.04 eV and for pure Cs_1PM, the E_g decreasing is 0.05 eV.

3.5. Thermal analysis

From the TG–DTA measurements of both Cs_1PM and Cs_3PM the following processes could be observed: the crystallization water elimination in several steps, the decomposition of the anhydrous samples by constitutive water removal (all accompanied by endothermic effects) and finally the crystallization process of constitutive oxides accompanied by exothermic effects [48,49].

In the region of the hydrated water elimination, the DTA curve of Cs_1PM shows two endothermic peaks at 60 and 85 °C (not shown), and Cs_3PM shows only one endothermic peak at 62 °C which may be assigned to bonded water from the crystal hydrates with different number of water molecules [48]. From TG and DTG curves it could be observed the loss of water of crystallization processes accompanied by a considerable weight loss. The final process evidenced by an exothermic peak over 500 °C is assigned to
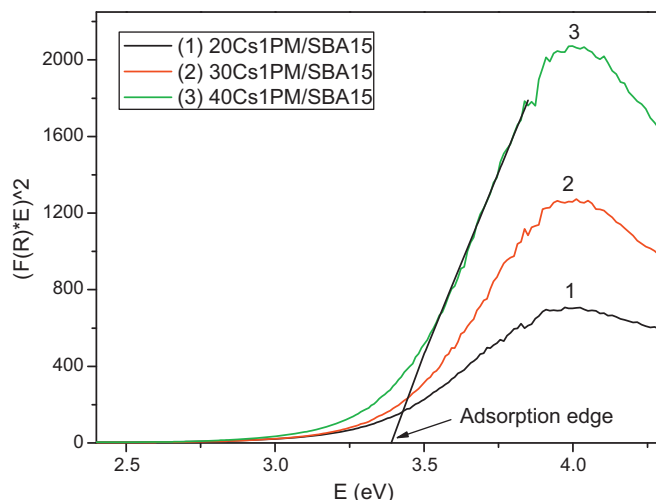

Fig. 8. The $[F(R) \times E]^2$ vs. E curves for Cs_1PM/SBA-15 composites.

Table 2
The band gap energy of $Cs_{3-x}H_xPMo_{12}O_{40}$/SBA15 composites ($x = 0; 2$).

Samples	Band gap determined by the relation: $[F(R) \cdot E]^2 = f(E)$ (eV)	
	30 °C	250 °C
Cs_1PM	2.87	2.82
20 Cs_1PM/SBA-15	3.31	3.27
30 Cs_1PM/SBA-15	3.38	3.36
40 Cs_1PM/SBA-15	3.41	3.39
Cs_3PM	3.21	3.17
20 Cs_3PM/SBA-15	3.26	3.25
30 Cs_3PM/SBA-15	3.33	3.31
40 Cs_3PM/SBA-15	3.36	3.34

the destruction of Keggin structure and crystallization of constitutive oxides: MoO_3 and P_2O_5.

Due to composites higher specific surface area (Table 1), the thermal behaviour in the temperature range corresponding to the elimination of the hydrated water of all CsPM/SBA-15 composites is quite different compared to the pure Cs salts. For instance, in the case of 20Cs$_1$PM/SBA-15 composite the endothermic effect (75 °C) is due to the additive thermal effects of the desorbed water from silica surface and to the loss of the HPA crystallization water (Fig. 9). The loss of the hydrated water is completed up to 150 °C.

In the temperature range 150–350 °C a slow and continuous loss of sample weight is proceeding, owing to the departure of water molecules of the Cs_1PM and probably to remaining traces of the organic surfactant used for preparation of mesoporous SBA-15. The constitutional water – which is formed from acidic protons and oxygen belonging to the Keggin units – are removed between 450 and 550 °C temperature range, this process being evidenced on DTG curve at 510 °C.

For all loadings of CsPM/SBA-15 composites an exothermic peak could be observed on DTA curve at a temperature higher than 600 °C. This exothermic peak could be assigned to the decomposition of active phase CsPM and crystallization of constitutive oxides resulted after decomposition.

The thermal effects of pure Cs salts and all CsPM/SBA-15 composites are better evidenced by DSC method. For 20Cs$_1$PM/ SBA-15 the exothermic peak assigned to the decomposition of active phase is observed at 638 °C, while for the other compositions this peak is observed at 622 °C (30Cs$_1$PM/SBA-15) and at 652 °C for 40Cs$_1$PM/SBA-15 composite (Fig. 10a).

Pure Cs_1PM is thermally less stable, the exothermic peak being observed at 509 °C on DSC curve. Therefore immobilization on
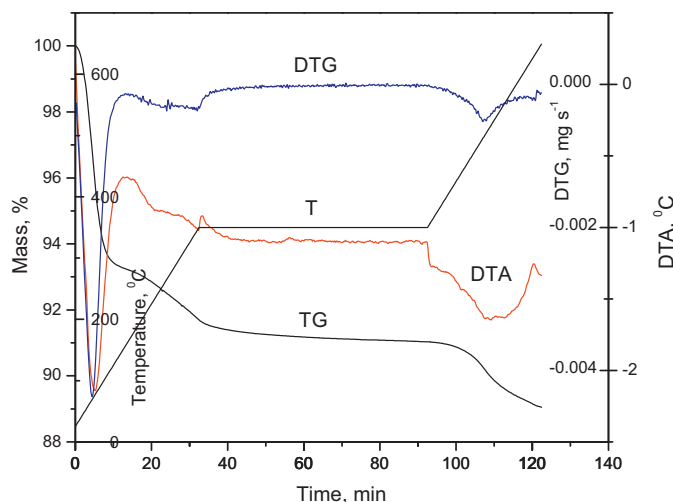
Fig. 9. TG–DTG and DTA curves of 20Cs$_1$PM/SBA-15 composites.
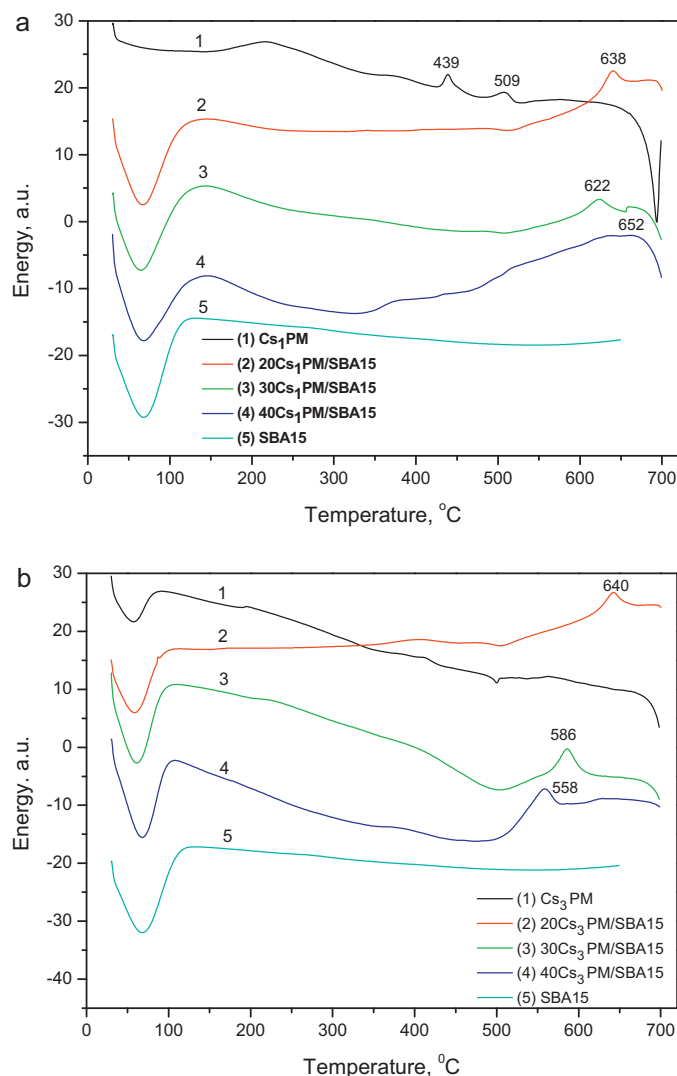
Fig. 10. (a) DSC analysis of Cs_1PM/SBA-15 composites and (b) DSC analysis of Cs_3PM/SBA-15 composites.

mesoporous SBA-15 obviously increases the thermal stability of the Keggin structures in comparison with their parent bulk Cs salts, probably due to the interaction of Cs_1PM with surface silanols on the support.

For 20Cs$_3$PM/SBA-15 the exothermic peak assigned to the decomposition of active phase is observed at 640 °C, while for the other compositions this peak is observed at 586 °C (30Cs$_3$PM/SBA-15) and at 558 °C for 40Cs$_3$PM/SBA-15 composite (Fig. 10b).

As in the other cases, neutral salt Cs_3PM is thermally less stable than supported ones, the exothermic peak being observed below 500 °C on DSC curve. Therefore immobilization on mesoporous SBA-15 obviously increases the thermal stability of the Keggin structures in comparison with their parent bulk Cs salts, probably related to the interaction of CsPM with surface silanols on the support.

3.6. The TPD measurements

Ammonia adsorption–desorption technique usually enables the determination of the amount of acidic sites and the strength of acid sites present on the catalyst surface together with the total acidity. The NH$_3$-TPD experiments were recorded as the TG - DTG and DTA curves (Fig. 11). This method was used previously for studying the
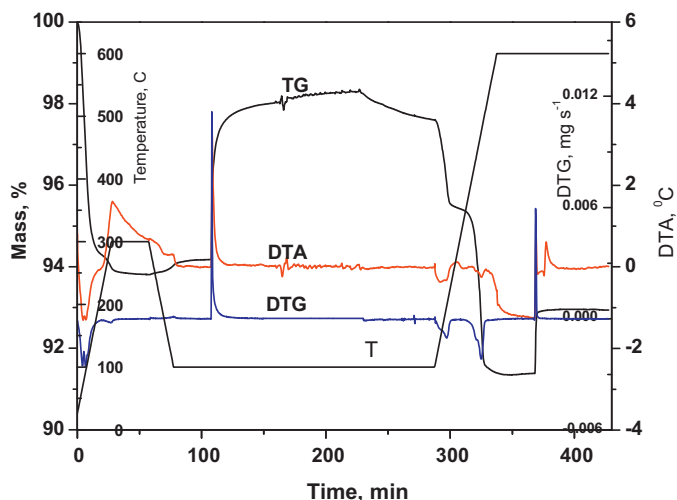
Fig. 11. Thermal curves recorded during crystallization water removal and adsorption/desorption of ammonia on Cs_1PM.
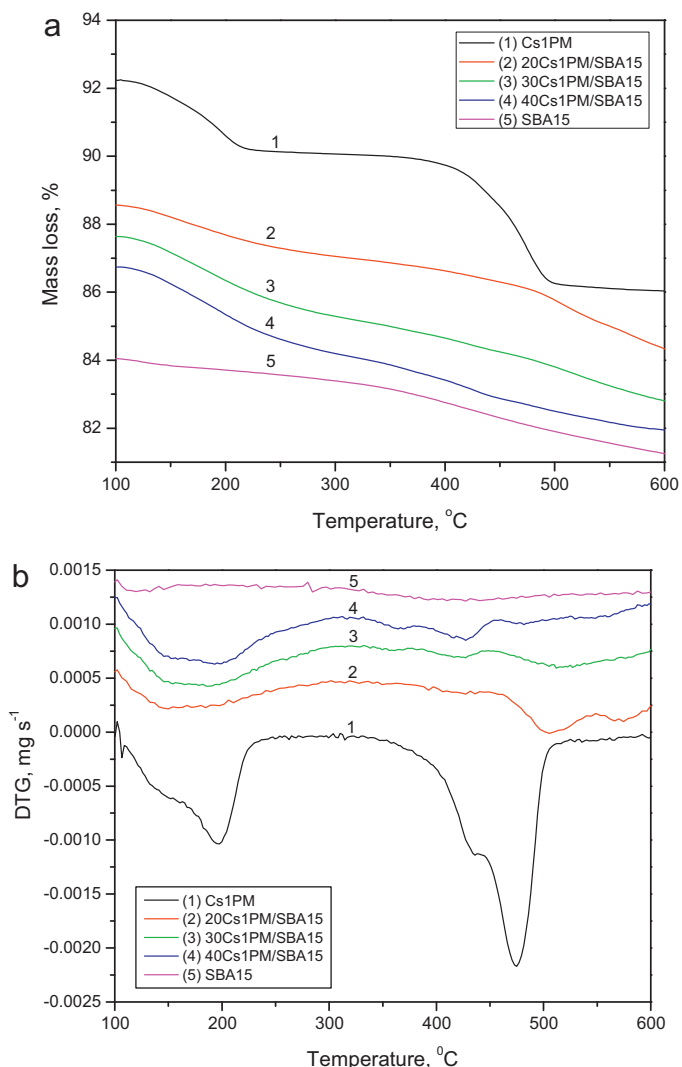

Fig. 12. (a) TPD of ammonia in the temperature range of 100–600 °C for Cs_1PM/SBA-15 composites (TG curves) and (b) TPD of ammonia in the temperature range of 100–600 °C for Cs_1PM/SBA-15 composites (DTG curves).

Brönsted acidities of the 12-tungstophosphoric acid and its Cs salts by using the TPD of ethanol and TPD of n-butyl amines [50,51].

From the TG–DTG and DTA curves is observed the crystallization water loss until 150–200 °C, followed by the isothermal heating at 300 °C, corresponding to the complete removal of crystallization water and the formation of anhydrous forms for HPAs. The assignment of mass loss for desorption and the calculations of desorbed quantities of ammonia were based on the TG, DTG and DTA curves for the non-isothermal heating in the range of 100–600 °C, shown in Fig. 12a and b. The results of TPD experiments for the desorption in the temperature range of 100–600 °C are collected in Table 3.

The strength of acid sites is related to the corresponding desorption temperature. Generally, the acid sites are classified into the weak (150–300 °C), medium (300–450 °C) and strong (450–600 °C) acid sites [12]. For pure Cs_1PM and Cs_1PM–SBA15 composites at least two NH_3 desorption steps were observed that were ascribed to weak, medium or strong acidic sites accordingly with Table 3. The NH_3 desorption of pure Cs_1PM has the first desorption maximum rate at 208 °C (weak acidic sites) and the 2nd with the desorption maximum rate at 488 °C (strong acidic sites). A shoulder is observed at 440 °C which is ascribed to the removal of constitutional water resulted from acidic protons of acidic Cs salt.

For Cs_1PM–SBA15 composites the desorption peaks ascribed to strong acidic sites are shifted to higher temperature (575 °C for $20Cs_1PM$–SBA15) which could be related to the strong acidic sites generated due to the presence of well-dispersed Keggin ions on silica.

No NH_3 desorption peak on DTG or mass loss on TG curve could be found for Cs_3PM, suggesting the total absence of acidic sites. The SBA-15 support shows a small and broad desorption peak centred around 250 °C corresponding to weak acidic sites. These acidic sites arise from surface hydroxyl group attached with Si. The same small and broad desorption peak cantered around 250 °C corresponding to weak acidic sites could be found for Cs_3PM–SBA15 composites.

Data in Table 3 show that the total acidity ($mmol/g_{cat}$) of pure Cs_1PM salt increased two times by supported on SBA-15. Also the total acidity ($mmol/g_{cat}$) of the strong acidic sites are increased for Cs_1PM–SBA15 composites especially for 20 and 30 wt.% loadings. But when calculating the density of acidic sites on the surface, the highest value, 334.4 $\mu mol/m_{cat}^2$, was obtained for pure Cs_1PM, which was related to its low specific surface area (6.04 m^2/g). Therefore, as expected, the amount and the distribution of the acid

strengths on the active phase were significantly influenced by the properties of the support.

3.7. SEM and EDX characterization

The morphology of CsPM/SBA-15 composites was studied by scanning electron microscopy technique and obtained micrograph is displayed in Fig. 13. Both Cs_1PM and Cs_3PM/SBA-15 composites have the morphology very similar to SBA-15 support. It is composed of rope like shape particles with an average diameter below 1 μm. The diameter size of the ropes is relatively uniform, and the ropes can be aggregated into wheat like macroscopic structures.

Active phase distribution over the surface of SBA-15 was analyzed by SEM-EDX method. In order to get representative composition of the composites, a minimum of four areas of about 500 $\mu m \times$ 500 μm were analyzed on each sample. The analysis was repeated on different particles of the same batch in order to ensure the reproducibility of the obtained results.

By this technique was obtained the chemical composition of silicon from SBA-15 and Mo, P and Cs elements from both Cs_1PM and Cs_3PM/SBA-15 composites. The data of EDX analysis for

Table 3
Amount of acidic sites and distribution of acid strengths.

Catalyst	Acidity, NH$_3$ uptake, μmol/m^2 cat (mmol/g cat)			Total acidity, μmol/m^2 (mmol/g)
	150–300 °C, weak	300–450 °C, medium	450–600 °C, strong	
Cs$_1$PM	125.8 (0.76)	–	208.6 (1.26)	334.4 (2.02)
20 Cs$_1$PM/SBA15	–	4.3 (1.88)	4.9 (2.18)	9.2 (4.06)
30 Cs$_1$PM/SBA15	–	1.3 (0.51)	8.9 (3.54)	10.2 (4.05)
40 Cs$_1$PM/SBA15	–	2.4 (0.77)	3.7 (1.18)	6.1 (1.95)
Cs$_3$PM	–	–	–	–
20 Cs$_3$PM/SBA15	Trace	–	–	Trace
SBA15	Trace	–	–	Trace

Table 4
Energy dispersive X-ray (EDX) analysis data for Cs, P and Mo in Cs$_{3-x}$H$_x$PMo$_{12}$O$_{40}$/SBA-15 composites ($x = 0$; 2).

Sample	Elemental analysis (wt.%)					
	Mo		P		Cs	
	Exp.	Stoich.	Exp.	Stoich.	Exp.	Stoich.
Cs$_1$PM	58.8	58.8	1.7	1.6	7.4	6.8
20 Cs$_1$PM/SBA-15	11.8	11.8	0.2	0.3	1.3	1.4
30 Cs$_1$PM/SBA-15	17.5	17.7	0.4	0.5	1.9	2.0
40 Cs$_1$PM/SBA-15	23.2	23.5	0.5	0.6	2.5	2.7
Cs$_3$PM	52.3	51.8	1.6	1.4	17.6	17.0
20 Cs$_3$PM/SBA-15	10.7	10.4	0.3	0.3	3.7	3.6
30 Cs$_3$PM/SBA-15	15.6	15.6	0.5	0.4	5.8	5.4
40 Cs$_3$PM/SBA-15	20.8	20.9	0.6	0.6	7.0	7.2
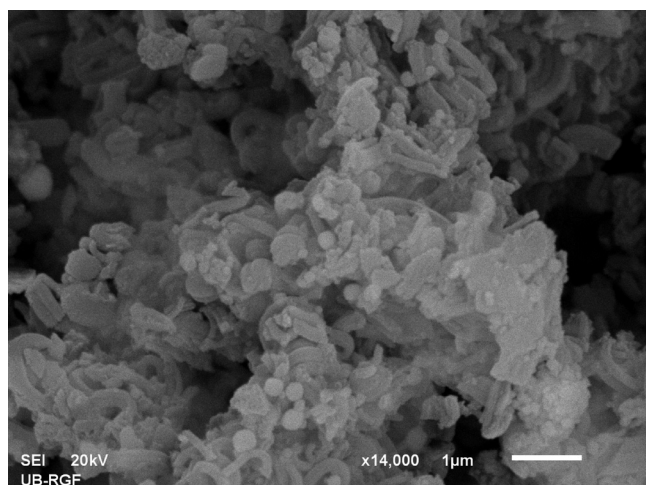
Fig. 13. SEM micrograph of 20 wt.% Cs$_3$PM/SBA-15.

Cs$_1$PM/SBA-15 composites show that the molybdenum, phosphorous and caesium content is relatively homogeneous and close to stoichiometric values. In the case of 20 Cs$_1$PM/SBA-15 composites the average content of Mo as wt.% is almost the same as stoichiometric one: 11.84 is experimental value and stoichiometric value is 11.77 wt.%. Also, P content (0.22 wt.%) and Cs content (1.32 wt.%) are close to stoichiometric values (Table 4).

For Cs$_3$PM/SBA-15 composites by comparing the experimental and stoichiometric values of Cs concentration values, it can be observed that for higher loadings of active phase (30 and 40%), the samples exhibit some small deviations from stoichiometric values. It could be supposed that active phase was less homogeneously dispersed inside the composite pores than for low loadings of active phase.

4. Conclusions

In this study is described a procedure for supporting insoluble Cs acid and neutral salts on mesoporous SBA-15 by two-step sequential impregnation with a variation of active phase content (20–40 wt.%).

The presence of Bragg peaks at small angles and a high surface area of CsPM/SBA-15 composites demonstrate that these materials have a mesoporous structure. However, from the XRD patterns of CsPM/SBA-15 composites it can be asserted that the long-range order of mesoporous SBA-15 is decreased especially for high loading of 40 wt.% CsPM.

FTIR and micro-Raman spectroscopy showed that CsPM retained its parent Keggin structure after supporting into the substrate. For both Cs$_1$PM and Cs$_3$PM/SBA-15 composites one could be observed an important increase of band gap energy in comparison with pure salts, which could be attributed to a structural distortion of the HPAs network due to support interaction or/and due to lower polarizing effect of the KU.

The immobilization of active phase on mesoporous SBA-15 obviously increases the thermal stability of the Keggin structures in comparison with their parent bulk Cs salts, probably due to the interaction of CsPM with surface silanols on the support. The total acidity (mmol/g$_{cat}$) of pure Cs$_1$PM salt increased two times by supported it on SBA-15. Also the total acidity (mmol/g$_{cat}$) of the strong acidic sites are increased for Cs$_1$PM–SBA15 composites especially for 20 and 30 wt.% loadings.

From SEM-EDS analysis it could be observed that for higher loadings of active phase the samples exhibit some small deviations of Mo and Cs concentration values from the stoichiometric ones. So, distribution of Cs salts over the surface of SBA-15 is more homogeneous for 20 wt.% loading.

References

[1] F. Cavani, Catal. Today 41 (1998) 73–86.
[2] N. Mizuno, M. Misono, Chem. Rev. 98 (1998) 199–217.
[3] G.D. Yadav, G. George, Catal. Today 141 (2009) 130–137.

[4] A. Popa, V. Sasca, J. Halasz, Appl. Surf. Sci. 255 (5) (2008) 1830–1835.
[5] Q.Y. Liu, W.L. Wu, J. Wang, X.Q. Ren, Y.R. Wang, Microporous Mesoporous Mater. 76 (2004) 51–60.
[6] R. Palcheva, A. Spojakina, L. Dimitrov, K. Jiratova, Microporous Mesoporous Mater. 122 (2009) 128–134.
[7] A. Popa, V. Sasca, E.E. Kiss, R. Marinkovic-Neducin, M.T. Bokorov, I. Holclajtner-Antunović, Mater. Chem. Phys. 119 (3) (2010) 465–470.
[8] A. Popa, V. Sasca, E.E. Kiss, R. Marinkovic-Neducin, I. Holclajtner-Antunović, Mater. Res. Bull. 46 (2011) 19–25.
[9] A. Popa, V. Sasca, E.E. Kiš, R. Marinkovic-Neducin, J. Halasz, J. Optoelectron. Adv. Mater. 10 (6) (2008) 1401–1407.
[10] A. Popa, N. Pleşu, V. Sasca, E.E. Kiš, R. Marinković-Nedučin, J. Optoelectron. Adv. Mater. 8 (5) (2006) 1944–1950.
[11] S. Soled, S. Miseo, G. McVicker, W.E. Gates, A. Gutierrez, J. Paes, Catal. Today 36 (1997) 441–480.
[12] F. Jing, B. Katryniok, E. Bordes-Richard, S. Paul, Catal. Today 203 (2013) 32–39.
[13] N. Essayem, G. Coudurier, M. Fournier, J.C. Védrine, Catal. Lett. 34 (1995) 223–235.
[14] A. Molnar, C. Keresszegi, B. Torok, Appl. Catal. A 189 (1999) 217–224.
[15] A. Kukovecz, Zs. Balogi, Z. Konya, M. Toba, P. Lentz, S.-I. Niwa, F. Mizukami, A. Molnar, J.B. Nagy, I. Kiricsi, Appl. Catal. A 228 (2002) 83–94.
[16] P.M. Rao, M.V. Landau, A. Wolfson, A.M. Shapira-Tchelet, M. Herskowitz, Microporous Mesoporous Mater. 80 (2005) 43–55.
[17] A. Molnar, T. Beregszaszi, A. Fudala, P. Lentz, J.B. Nagy, Z. Konya, I. Kiricsi, J. Catal. 202 (2001) 379–386.
[18] J.S. Santos, J.A. Dias, S.C.L. Dias, F.A.C. Garcia, J.L. Macedo, F.S.G. Sousa, L.S. Almeida, Appl. Catal. A 394 (2011) 138–148.
[19] V. Sydorchuk, V. Zazhigalov, S. Khalameida, J. Skubiszewska-Zięba, B. Charmas, R. Leboda, Colloids Surf. A 341 (1–3) (2009) 53–59.
[20] C. Yuan, J. Chen, Chin. J. Catal. 32 (2011) 1191–1198.
[21] X. Sheng, Y. Zhou, Y. Zhang, M. Xue, Y. Duan, Chem. Eng. J. 179 (2012) 295–301.
[22] L. Yang, Y. Qi, X. Yuan, J. Shen, J. Kim, J. Mol. Catal. A: Chem. 229 (1/2) (2005) 199–205.
[23] V.V. Bokade, G.D. Yadav, Appl. Clay Sci. 53 (2011) 263–271.
[24] L. Lizama, T. Klimova, Appl. Catal. B 82 (2008) 139–150.
[25] A.I. Tropecêlo, M.H. Casimiro, I.M. Fonseca, A.M. Ramos, J. Vital, J.E. Castanheiro, Appl. Catal. A 390 (2010) 183–189.
[26] R. Wei, M. Guo, J. Wang, Chin. J. Chem. Eng. 17 (1) (2009) 58–63.
[27] J.B. Moffat, Metal-Oxygen Clusters: The Surface and Catalytic Properties of Heteropoly Oxometalates, Springer, New York, 2001.
[28] J. Haber, L. Matachowski, D. Mucha, J. Stoch, P. Sarv, Inorg. Chem. 44 (2005) 6695–6703.
[29] M. Misono, Chem. Commun. 13 (2001) 1141–1152.
[30] P.Y. Gayraud, N. Essayem, J. Vedrine, Catal. Lett. 56 (1998) 35–41.
[31] I. Holclajtner-Antunovic, U.B. Mioc, M. Todorovic, Z. Jovanovic, M. Davidovic, D. Bajuk-Bogdanovic, Z. Lausevic, Mater. Res. Bull. 45 (2010) 1679–1684.
[32] I.V. Kozhevnikov, Catalysis for Fine Chemical Syntheses – Catalysis by Polyoxometalates, vol. 2, John Wiley & Sons, Ltd, Chichester, 2002.
[33] S. Gong, L. Liu, Q. Cui, J. Ding, J. Hazard. Mater. 178 (2010) 404–408.
[34] A. Popa, V. Sasca, I. Holclajtner-Antunovic, Microporous Mesoporous Mater. 156 (2012) 127–137.
[35] D. Zhao, J. Feng, Q. Huo, N. Melosh, G.H. Fredrickson, B.F. Chmelka, G.D. Stucky, Science 279 (1998) 548–552.
[36] D. Zhao, J. Sun, Q. Li, G.D. Stucky, Chem. Mater. 12 (2000) 275–279.
[37] K.S.W Sing, D.H. Everett, R.A.W. Haul, L. Moscou, R.A. Pierotti, J. Rouquerol, T. Siemieniewska, Pure Appl. Chem. 57 (1985) 603–619.
[38] T. Okuhara, T. Nakato, Catal. Surv. Jpn. 2 (1998) 31–44.
[39] V.Z. Sasca, O. Verdes, L. Avram, A. Popa, A. Erdöhelyi, A. Oszko, Appl. Catal. A 451 (2013) 50–57.
[40] M.T. Pope, Heteropoly and Isopoly Oxometalates, Springer-Verlag, Berlin, 1983.
[41] A.J. Bridgeman, Chem. Phys. 287 (2003) 55–69.
[42] C. Rocchiccioli-Deltcheff, M. Fournier, R. Frank, R. Thouvenot, Inorg. Chem. 22 (1983) 207–216.
[43] C. Rocchiccioli-Deltcheff, A. Aouissi, M.M. Bettahar, S. Launay, M. Fournier, J. Catal. 164 (1996) 16–27.
[44] M. Fournier, C. Louis, M. Che, P. Chaquin, D. Masure, J. Catal. 119 (1989) 400–414.
[45] D. Masure, P. Chaquin, C. Louis, M. Che, M. Fournier, J. Catal. 119 (1989) 415–425.
[46] K. Brückman, M. Che, J. Haber, J.M. Tatibouët, Catal. Lett. 25 (1994) 225–240.
[47] R.S. Weber, J. Catal. 151 (1995) 470–474.
[48] V. Sasca, M. Stefanescu, A. Popa, J. Therm. Anal. Calorim. 56 (1999) 569–578.
[49] A. Popa, V. Sasca, M. Stefanescu, E.E. Kis, R. Marinkovic-Neducin, J. Serb. Chem. Soc. 71 (3) (2006) 235–249.
[50] V. Sasca, L. Avram, O. Verdes, A. Popa, Appl. Surf. Sci. 256 (17) (2010) 5533–5538.
[51] O. Verdes, L. Avram, A. Popa, V. Sasca, J. Optoelectron. Adv. Mater. 14 (5/6) (2012) 537–543.